Microfluid Nanofluid (2016) 20:140
DOI 10.1007/s10404-016-1803-5

RESEARCH PAPER

Three-dimensional simulations of viscous folding in diverging microchannels

Bingrui XU[1,2] · **Jalel Chergui**[2] · **Seungwon Shin**[3] · **Damir Juric**[2]

Received: 21 April 2016 / Accepted: 12 September 2016 / Published online: 26 September 2016

Abstract Three-dimensional simulations on the viscous folding in diverging microchannels reported by Cubaud and Mason (Phys Rev Lett 96(11):114,501, 2006a) are performed using the parallel code BLUE for multiphase flows (Shin et al. in A solver for massively parallel direct numerical simulation of three-dimensional multiphase flows. arXiv:1410.8568). The more viscous liquid L_1 is injected into the channel from the center inlet, and the less viscous liquid L_2 from two side inlets. Liquid L_1 takes the form of a thin filament due to hydrodynamic focusing in the long channel that leads to the diverging region. The thread then becomes unstable to a folding instability, due to the longitudinal compressive stress applied to it by the diverging flow of liquid L_2. Given the long computation time, we were limited to a parameter study comprising five simulations in which the flow rate ratio, the viscosity ratio, the Reynolds number, and the shape of the channel were varied relative to a reference model. In our simulations, the cross section of the thread produced by focusing is elliptical rather than circular. The initial folding axis can be either parallel or perpendicular to the narrow dimension of the chamber. In the former case, the folding slowly transforms via twisting to perpendicular folding, or it may remain parallel. The direction of folding onset is determined by the velocity profile and the elliptical shape of the thread cross section in the channel that feeds the diverging part of the cell. Due to the high viscosity contrast and very low Reynolds numbers, direct numerical simulations of this two-phase flow are very challenging and to our knowledge these are the first three-dimensional direct parallel numerical simulations of viscous threads in microchannels. Our simulations provide good qualitative comparison of the early time onset of the folding instability, however, since the computational time for these simulations is quite long, especially for such viscous threads, long-time comparisons with experiments for quantities such as folding amplitude and frequency are limited.

Keywords Three dimensional · Viscous folding · Diverging microchannel

1 Introduction

The folding of viscous threads in diverging microchannels has recently attracted much attention due to the need to mix two fluids with very different viscosities. The dynamics of viscous multiphase flows at small scales is important in industrial technology (oil recovery, biodiesel production, etc.). Microfluidic devices are well suited for studying precisely controlled flow geometries and finely manipulating the fluid and can be used to produce individual bubbles, droplets, and complex soft materials (Utada et al. 2005; Cubaud et al. 2005; Meleson et al. 2004). The effective mixing is of great importance in these various microfluidic applications. But microfluidic flows are usually laminar, so liquid streams are parallel and different fluids can only

---

✉ Bingrui XU
xu@fast.u-psud.fr

Jalel Chergui
jalel.chergui@limsi.fr

Damir Juric
damir.juric@limsi.fr

[1] Laboratoire FAST, Université Paris-Sud, CNRS, Université Paris-Saclay, 91405 Orsay, France

[2] LIMSI, CNRS, Université Paris-Saclay, 91405 Orsay, France

[3] Department of Mechanical and System Design Engineering, Hongik University, Seoul 121-791, Republic of Korea

mix by diffusion. The time scale associated with diffusion, $t_d = h^2/D$, where h is the characteristic length scale and D is the diffusion coefficient between the liquids, is typically much larger than the time scale associated with convection, $t_c = h/U$, where U is the characteristic flow velocity. Therefore, diffusion alone is an extremely inefficient mixing method.

There are different innovative strategies to enhance mixing in microfluidics, which can be classified as either active or passive methods. In active methods, an external forcing is imposed by, e.g., rotary pumps (Chou et al. 2001), forced oscillatory transverse flows (Bottausci et al. 2004), or electric or magnetic fields (Paik et al. 2003a, b; Pollack et al. 2002; Kang et al. 2007a, b; Rida and Gijs 2004). Passive methods rely on a particular design of the microchannel, including patterned surface relief (Chen et al. 2009; Bringer et al. 2004; Stroock et al. 2002a, b). However, industrial and biological fluids usually exhibit widely different viscosities and the relative motions between the fluids are complex. In this article, we study one promising method, wherein periodic folding of viscous threads injected into microchannels enhances mixing by greatly increasing the specific surface area of the fluid/fluid interface.

The buckling (folding or coiling) of slender viscous threads is familiar to anyone who has ever poured honey or molten chocolate onto toast. Taylor (1969) investigated the viscous buckling problem and suggested that the instability requires an axial compressive stress, like the more familiar 'Euler' buckling of a compressed elastic rod. Since then, viscous buckling has been studied by numerous authors using experimental, theoretical, and numerical approaches (Cruickshank and Munson 1982a, b, 1983; Cruickshank 1988; Griffiths and Turner 1988; Tchavdarov et al. 1993; Mahadevan et al. 1998; Skorobogatiy and Mahadevan 2000; Tome and Mckee 1999; Ribe 2004; Ribe et al. 2006; Maleki et al. 2004; Habibi et al. 2014; Brun et al. 2014). The primary result of this work is that buckling can occur in four distinct modes (viscous, gravitational, inertio-gravitational, and inertial) depending on the force that balances the viscous resistance to bending as a function of fall height.

With the exception of Griffiths and Turner (1988), all the studies cited above consider 'non-immersed' folding/coiling that occurs when the influence of the external fluid (typically air in experiments) is negligible. Recently, Cubaud and Mason (2006a) have studied the immersed buckling that occurs when two fluids with different viscosities are injected into a diverging microchannel. The thread is produced by hydrodynamic focusing of a viscous fluid flow by a less viscous fluid injected from the sides. Silicone oils with different viscosities were used to obtain different viscosity ratios. On the basis of their experimental results, Cubaud and Mason (2006a) proposed that $f \sim \dot{\gamma}$, where f is the folding frequency and $\dot{\gamma} = U_1/(h/2)$ is the characteristic shear rate. The thread of radius R_1 can be assumed to flow at nearly constant velocity, $U_1 = Q_1/(\pi R_1^2)$, like a solid plug, inside a sheath of the less viscous liquid, similar to the flow in a circular channel. In this case, U_1 represents the maximum velocity of the surrounding liquid. Downstream, the thread and surrounding liquid enter the diverging channel creating a decelerating extensional flow. Extensional viscous stresses cause the thread to bend and fold, rather than dilate, in order to minimize dissipation and conserve mass. As the thread folds, it reduces its velocity and mixes with the outer liquid. In addition to folding, many other potentially useful flow phenomena are obtained, including oscillatory folding, folding modified by strong diffusion, heterogeneous folding, and subfolding (Cubaud and Mason 2006b).

Chung et al. (2010) performed numerical and experimental studies on viscous folding in diverging microchannels similar to those of Cubaud and Mason (2006a). However, it is important to note that the numerical simulations of Chung et al. (2010) are two dimensional, unlike their or Cubaud's experiments which are fully three dimensional. Chung et al. (2010) obtained a regime diagram for the flow pattern observed (stable, folding, or chaotic) as a function of the flow rate ratio, the viscosity ratio, and the channel shape. In addition to the divergence angles $\alpha = \pi/2$ and $\alpha = \pi$, Chung et al. (2010) also performed simulations for a channel with walls of hyperbolic shape, to obtain a more uniform compressive stress along the channel's centerline. The hyperbolic channel generated folding flows with smaller frequency and amplitude, as well as a delay of onset of the folding. There are two main differences between Chung's simulations and Cubaud's experiments. First, Chung et al. (2010) found the existence of an upper bound of viscosity ratio for folding instability. Secondly, Chung et al. (2010) obtained a power-law relation $f \sim \dot{\gamma}^{1.68}$, which is quite different from the Cubaud and Mason (2006a) law $f \sim \dot{\gamma}$.

For fluids with a large viscosity ratio, the thread generated by hydrodynamic focusing requires a long focusing channel to become thin. The existence of an upper bound of viscosity ratio for the folding instability could be owed to the thick thread, because the focusing channel is short in the study of Chung et al. (2010). Three-dimensional simulations promise to be helpful in understanding such details of the viscous folding phenomenon. To this end, we use the parallel code BLUE for multiphase flow based on the front tracking method (developed by Shin et al. 2014) to simulate three-dimensional viscous folding in diverging microchannels. The computational domain includes a focusing channel sufficiently long to allow the full formation of threads as in the experiments of Cubaud and Mason (2006a).

2 Methods

2.1 Mathematical formulation

Here, we describe the basic solution procedure for the Navier–Stokes equations with a brief explanation of the interface method. The governing equations for an incompressible two-phase flow can be expressed by a single field formulation as follows:

$$\nabla \cdot u = 0, \tag{1}$$

$$\rho\left(\frac{\partial u}{\partial t} + u \cdot \nabla u\right) = -\nabla P + \rho g + \nabla \cdot \eta(\nabla u + \nabla u^T) + F. \tag{2}$$

where ρ is the density, u is the velocity, P is the pressure, g is the gravitational acceleration, η is the viscosity, and F is the local surface tension force at the interface.

The fluid properties such density or viscosity are defined in the entire computational domain:

$$\rho(x,t) = \rho_1 + (\rho_2 - \rho_1)I(x,t), \tag{3}$$

$$\eta(x,t) = \eta_1 + (\eta_2 - \eta_1)I(x,t). \tag{4}$$

Where the subscripts 1 and 2 stand for the respective phases. The indicator function $I(x,\ t)$, a numerical Heaviside function, is zero in one phase and unity in the other phase. Numerically, I is resolved with a sharp but smooth transition across 3 to 4 grid cells and is generated using a vector distance function computed directly from the tracked interface (Shin and Juric 2009a, b).

The surface tension F can be described by the hybrid formulation

$$F = \sigma \kappa_H \nabla I, \tag{5}$$

where σ is the surface tension coefficient, κ_H is twice the mean interface curvature field calculated on the Eulerian grid using

$$\kappa_H = \frac{F_L \cdot G}{\sigma G \cdot G}, \tag{6}$$

$$F_L = \int_{\Gamma(t)} \sigma \kappa_f n_f \delta_f (x - x_f) \mathrm{d}s, \tag{7}$$

$$G = \int_{\Gamma(t)} n_f \delta_f (x - x_f) \mathrm{d}s. \tag{8}$$

Here, x_f is a parameterization of the interface $\Gamma(t)$, and $\delta(t)$ is a Dirac distribution that is nonzero only when $x = x_f$. n_f is the unit normal vector to the interface and ds is the length of the interface element. κ_f is again twice the mean interface curvature, but obtained from the Lagrangian interface structure. The geometric information, unit normal n_f and length of the interface element ds in G, F are computed directly from the Lagrangian interface and then distributed onto an Eulerian grid using the discrete delta function. The details following Peskin's (Peskin 1977) well-known immersed boundary approach and a description of our procedure for calculating the force F and constructing the function field G can be found in Shin and Juric (2007).

The Lagrangian elements of the interface are advected by integrating

$$\frac{\mathrm{d}x_f}{\mathrm{d}t} = V \tag{9}$$

with a second-order Runge–Kutta method where the interface velocity V is interpolated from the Eulerian velocity.

2.2 Numerical method

The treatment of the free surface uses the Level Contour Reconstruction Method (LCRM), a hybrid Front Tracking/Level Set technique. The LCRM retains the usual features of classic Front Tracking: to represent the interface with a triangular surface element mesh, to calculate the surface tension and advect it. A major advantage of the LCRM, compared with standard Front Tracking, is that all the interfacial elements are implicitly instead of logically connected. The LCRM periodically reconstructs the interface elements using a distance function field, such as the one in the Level Set method, thus allowing an automatic treatment of interface element restructuring and topology changes without the need for logical connectivity between interface elements.

The Navier–Stokes solver computes the primary variables of velocity u and pressure P on a fixed and uniform Eulerian mesh by means of Chorins projection method (Chorin 1968) with implicit solution of velocity. For the spatial discretization, we use the well-known staggered mesh, MAC method (Harlow et al. 1965). The pressure and the distance function are located at cell centers, while the components of velocity are located at cell faces. All spatial derivatives are approximated by standard second-order centered differences.

The code structure consists essentially of two main modules: (1) a module for solution of the incompressible Navier–Stokes equations and (2) a module for the interface solution including tracking the phase front, initialization and reconstruction of the interface when necessary. The parallelization of the code is based on algebraic domain decomposition, where the velocity field is solved by a parallel generalized minimum residual (GMRES) method for the implicit viscous terms and the pressure by a parallel multigrid method motivated by the algorithm of Kwak and

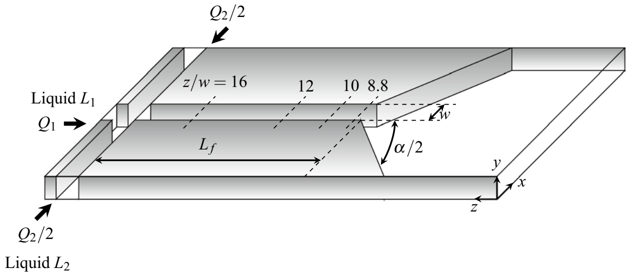

Fig. 1 The calculation domain of the microchannel. The width of the inlets and the microchannel is w and the length of the focusing microchannel is L_f. Four different position at $z/w = 8.8$, $z/w = 10$, $z/w = 12$ and $z/w = 16$ are indicated by the *dashed lines*

Lee (2003). Communication across process threads is handled by message passing interface (MPI) procedures.

Further detailed informations can be found in Shin et al. (2014).

2.3 Problem definition

Figure 1 shows the computational domain, whose geometry is similar to that used by Cubaud and Mason (Cubaud and Mason 2006a). The computational domain is composed of two subdomains: the flow-focusing part and the flow-diverging part. The more viscous liquid L_1 with viscosity η_1 is injected into the channel from the center inlet at a volumetric rate Q_1, and the less viscous liquid L_2 with viscosity η_2 from two side inlets at a total volumetric rate Q_2. The interfacial tension between two liquids is γ. In our simulations, the width of the inlets and the microchannel is $w = 0.25$ mm rather than 0.1 mm in Cubaud's experiments (Cubaud and Mason 2006a). The dimensions of the simulation domain are $8w \times w \times 20w$ (i.e., $2 \times 0.25 \times 5$ mm). Moreover, the length of the long focusing channel is $L_f = 10w = 2.5$ mm to obtain well-developed threads like Cubaud's another work (Cubaud et al. 2011). We use a Neumann boundary condition on the outlet, where the velocity derivatives are set to 0.

Some important dimensionless numbers are defined as follows:

$$\chi = \frac{\eta_1}{\eta_2}, \tag{10}$$

$$\phi = \frac{Q_1}{Q_2}, \tag{11}$$

$$\mathrm{Re}_1 = \frac{\rho_1 L V_1}{\eta_1}, \tag{12}$$

$$\mathrm{Re}_2 = \frac{\rho_2 L V_2}{\eta_2}, \tag{13}$$

Table 1 Dimensional and nondimensional parameters for the simulation case 1 with $\chi = 2174$, $\phi = 1/12$ and $\alpha = \pi/2$

Variables	Units	Values
ρ	kg/mm^3	0.8×10^{-6}
η_1	kg/mm/s	4864.28×10^{-6}
η_2	kg/mm/s	2.24×10^{-6}
Q_1	mm^3/s	0.83333
Q_2	mm^3/s	10
γ	kg/s^2	2.55×10^{-3}
Re_1		2.74×10^{-4}
Re_2		3.57
Ca_1		330.64
Ca_2		0.15
ϕ		1/12
χ		2174
α		$\pi/2$

$$\mathrm{Ca}_1 = \frac{\eta_1 \bar{V}}{\gamma}, \tag{14}$$

$$\mathrm{Ca}_2 = \frac{\eta_2 \bar{V}}{\gamma}. \tag{15}$$

Here χ is the viscosity ratio of two liquid, ϕ is the flow rate ratio. Re_1 and Re_2 are the Reynolds numbers of liquid L_1 and L_2, respectively, where the characteristic length scale $L = 0.5w$ and the characteristic velocities V_1 and V_2 are the average velocities and can be calculated from the volume flow flux and geometry parameters $V_1 = Q_1/w^2$ and $V_2 = 0.5Q_2/w^2$. The capillary numbers Ca_1 and Ca_2 are calculated in the long focusing channel, and the characteristic velocity is the average velocity in this long channel as $\bar{V} = (Q_1 + Q_2)/w^2$. Furthermore, we designed different channel geometries with two different diverging angles $\alpha = \pi$ and $\alpha = \pi/2$ for the main chamber.

A reference simulation (case 1) is chosen, and its detailed parameters and dimensionless numbers are shown in Table 1. In our parameter study, five simulations are performed. The dimensionless quantities for these cases are given in Table 2. In all five simulations, the capillary number Ca_1 is kept constant at 330.64, and the surface tension force is small compared to the viscous force for the liquid L_1. All the simulations are implemented using 64 ($4 \times 2 \times 8$) computational cores (subdomains) in parallel, and for each subdomain we use a $64 \times 32 \times 64$ mesh resolution. So the global mesh resolution for the domain is $256 \times 64 \times 512$, the grid size is $w/32 \times w/64 \times 5w/128$. Thus, the ratio between the maximum grid size and the channel width is $5/128 \approx 0.04$, and there are adequate grids in the microchannels. We have also done these simulations

Table 2 Dimensional and nondimensional parameters for the five simulations

Cases	Re_1	ϕ	χ	α
1 (reference)	2.74×10^{-4}	1/12	2174	$\pi/2$
2	1.64×10^{-3}	1/12	2174	$\pi/2$
3	2.74×10^{-4}	1/12	1000	$\pi/2$
4	2.74×10^{-4}	1/5	2174	$\pi/2$
5	2.74×10^{-4}	1/12	2174	π

under lower mesh resolution (half as much). By comparing the results of high resolution and low resolution, we think the mesh resolution 256 × 64 × 512 here is enough.

3 Numerical results

3.1 Thread formation

In our simulations, the threads are produced by hydrodynamic focusing. The liquid is injected from a central channel, and flows that ensheath the liquid are introduced from side channels. Downstream from the junction, the fluids flow side by side, and the width and location of the stream can be controlled through the injection flow rates. The hydrodynamic focusing technique provides an effective means of controlling the passage of chemical reagent or bio-samples through microfluidic channels and has given rise to many studies aimed at understanding its physical mechanisms. Various flow-geometry relationships have been studied to create different effects, including the influence of the channel aspect ratio (Lee et al. 2006), the injection geometry for detaching the central stream from the walls (Simonnet and Groisman 2005; Chang et al. 2007), the fluid driving mechanisms (Stiles et al. 2005) and the effect of small and moderate viscosity contrasts between the fluids (Wu and Nguyen 2005).

The more viscous liquid L_1 passes the junction and begins to detach from the top and bottom walls. The irregular shapes on the thread near the inlet are due to graphical artefacts. The contact line has a 'V'-like shape which is strongly stretched at the bottom. After the detachment from the walls, the liquid L_1 becomes thinner to form a thread. To analyze the focusing process more clearly, four cross sections across the depth at different positions $z/w = 8.8$, $z/w = 10$, $z/w = 12$ and $z/w = 16$ (case 2) are shown in Fig. 2.The liquid L1 flows at an almost uniform velocity (plug flow) at the beginning of hydrodynamic focusing and is accelerated by the side flow. The thread becomes thinner (from Fig. 2a–c) and then is nearly stable (from Fig. 2c, d). Moreover, it is noted that the cross section of the thread is an ellipse rather than a circle.

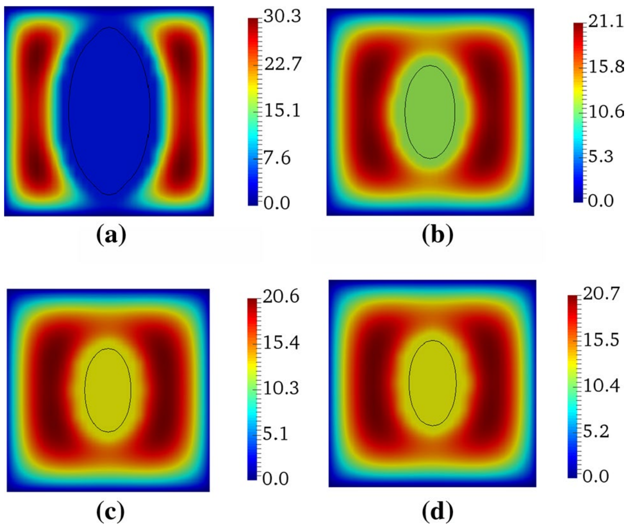

Fig. 2 The dimensionless velocity (V/V_1) *contour* of cross sections across the depth at different positions **a** $z/w = 16$, **b** $z/w = 12$, **c** $z/w = 10$ and **d** $z/w = 8.8$ for case 2 ($\mathrm{Re}_1 = 1.64 \times 10^{-3}, \phi = 1/12, \chi = 2174, \alpha = \pi/2$), the *black line* is the thread interface

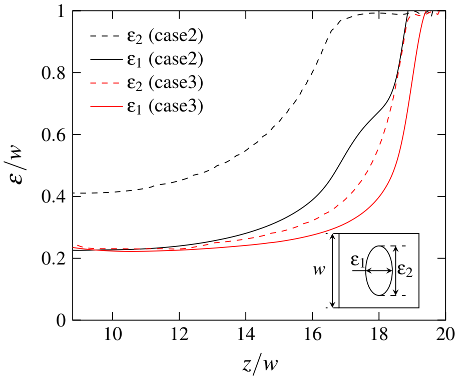

Fig. 3 The minor axis ε_1 and major axis ε_2 of the thread along the flow direction for case 2 ($\mathrm{Re}_1 = 1.64 \times 10^{-3}, \phi = 1/12, \chi = 2174, \alpha = \pi/2$) and case 3 ($\mathrm{Re}_1 = 2.74 \times 10^{-4}, \phi = 1/12, \chi = 1000, \alpha = \pi/2$)

To be clear, the minor axis of the thread ε_1 and the major axis of the thread ε_2 along the flow direction up to the diverging point are plotted in Fig. 3. The final developed state of the hydrodynamic focusing (the stretching) should have the maximum velocity at the centerline. Due to the large viscosity ratio here, this focusing process needs a very long channel to be complete. It is shown in Fig. 3 that the stretching or thinning of the thread is dramatic at the beginning of the focusing process, then become smaller and smaller. Finally, the stretching will vanish to the final state and the shape of the thread will become stable if the focus microchannel is much longer. Though the stretching

Table 3 The minor and major axes ε_1 and ε_2, their ratios $\varepsilon_1/\varepsilon_2$, and ratios with the inlet width ε_1/w and ε_2/w of the stable thread produced by focusing for all five cases

Cases	ε_1 (mm)	ε_2 (mm)	ε_1/w	ε_2/w	$\varepsilon_1/\varepsilon_2$
1 (base case)	0.0573	0.0836	0.2292	0.3344	0.69
2	0.0565	0.103	0.226	0.412	0.55
3	0.0578	0.057	0.2312	0.228	1.01
4	0.088	0.111	0.352	0.444	0.793
5	0.06	0.088	0.24	0.352	0.73

still exists in our simulations (in Fig. 2d), the thinning of the thread has been small enough and the shape of the thread varies little downstream in Fig. 3. Thus, a well-developed thread is obtained in our simulations and the width of this thread can be assumed as the one of the thread at final state. From Fig. 3, the stable minor axis and major axis of the thread produced by focusing are $\varepsilon_1/w = 0.226$ and $\varepsilon_2/w = 0.412$ for case 2. Besides, it suggests that liquid L_1 detaches completely from the walls near the position $z/w = 16.8$. The minor axis and major axis of the thread as well as the ratios ε_1/w, ε_2/w and $\varepsilon_1/\varepsilon_2$ for all five cases are listed in Table 3.

According to the velocity profile for the annular flow in a circular tube of diameter R directly calculated from the Stokes equations (Joseph and Renardy 1993), a simple scaling for the thread can be found with small threads $\varepsilon_c/w \ll 1$ and large viscosity ratios $\chi^{-1} \ll 1$: $\varepsilon_c/R \sim (\phi/2)^{0.5}$. Although this analysis is only valid for a circular tube, Cubaud (Cubaud and Mason 2009) suggests that the relationship between ε_c/w and ϕ is essentially the same for square tubes when $\chi^{-1} \ll 1$ and scales $\varepsilon_c/w \sim (\phi/2)^{0.5}$ as for small threads. For the case of a square micro channel of width w, ε_c/w for comparing circular diameter and square cross section instead of ε_c/R is used. It is noted that the thread is assumed circular, so ε_c is used as the diameter of the thread. Cubauds experiments (Cubaud and Mason 2006a) suggest that the thread minor axis (diameter) ε_1/w was independent of χ and follows $\varepsilon_1/w \sim \phi^{0.6}$. In Cubaud's experiments, they took photos from above with a high-speed camera, so that only the minor axis (diameter) ε_1 of the thread could be measured (Thus, it is not clear whether the thread cross section was circular or not). In Fig. 4, the estimating lines $\varepsilon_c/w \sim (\phi/2)^{0.5}$, $\varepsilon_1/w \sim \phi^{0.6}$ and values ε_1/w, ε_2/w from our simulations are presented. When ϕ is small, the two power-law predictions are close. From Fig. 4a, the slope of ε_1/w from our simulation results agrees well with both power-law relationships $\varepsilon_c/w \sim (\phi/2)^{0.5}$ and $\varepsilon_1/w \sim \phi^{0.6}$, the minor axis (the thread width from the top view) is only dependent on the flow ratio ϕ. However, for the major axis ε_2 of the thread in Fig. 4b, the situation seems more complicated in that ε_2/w depends on not only the flow rate ratio ϕ but also on other parameters such as the viscosity ratio χ. For the same ϕ, the lower viscosity ratio χ decreases the major axis and the thread cross section appears more circular.

As explained above, the cross section of threads become almost stable at $z/w = 10$ (case 2) and $z/w = 12$ (case 3) in Fig. 3. The long focusing microchannel is necessary for fluids with a large viscosity ratio to produce a thread thin enough. Chung et al. (2010) found the thread width ε_1/w also increased with increasing viscosity ratio χ and predicts the existence of the upper bound of χ for viscous folding. This is due to the short focusing microchannel, only $2w$ in their study. Consequently, the hydrodynamic focusing procedure is not completely finished and the thread is too thick

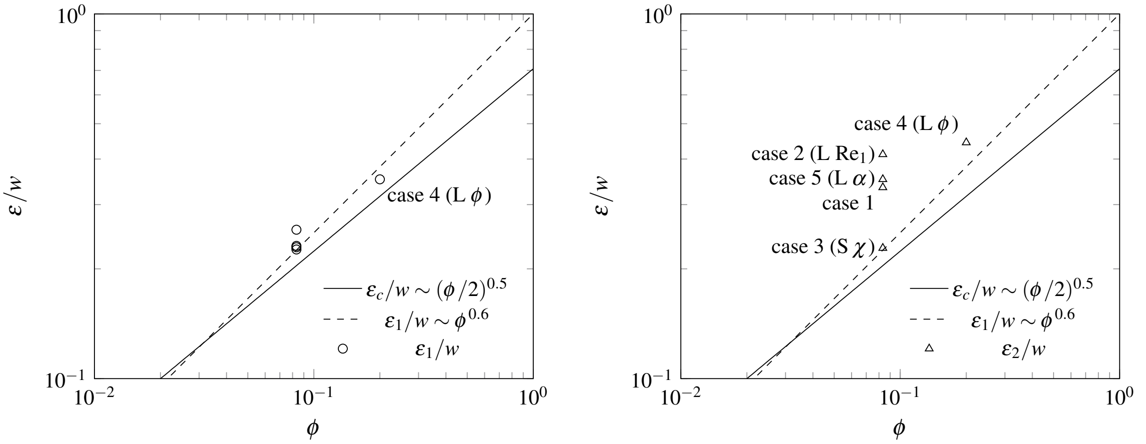

(a) **(b)**

Fig. 4 The ratio ε/w versus flow rate ratio ϕ for a thread in plug flow in a square microchannel. The *solid* and *dashed lines* are the power-law predictions, and the *circle* and *triangle marks* are ε_1/w and ε_2/w, respectively, from our simulation results

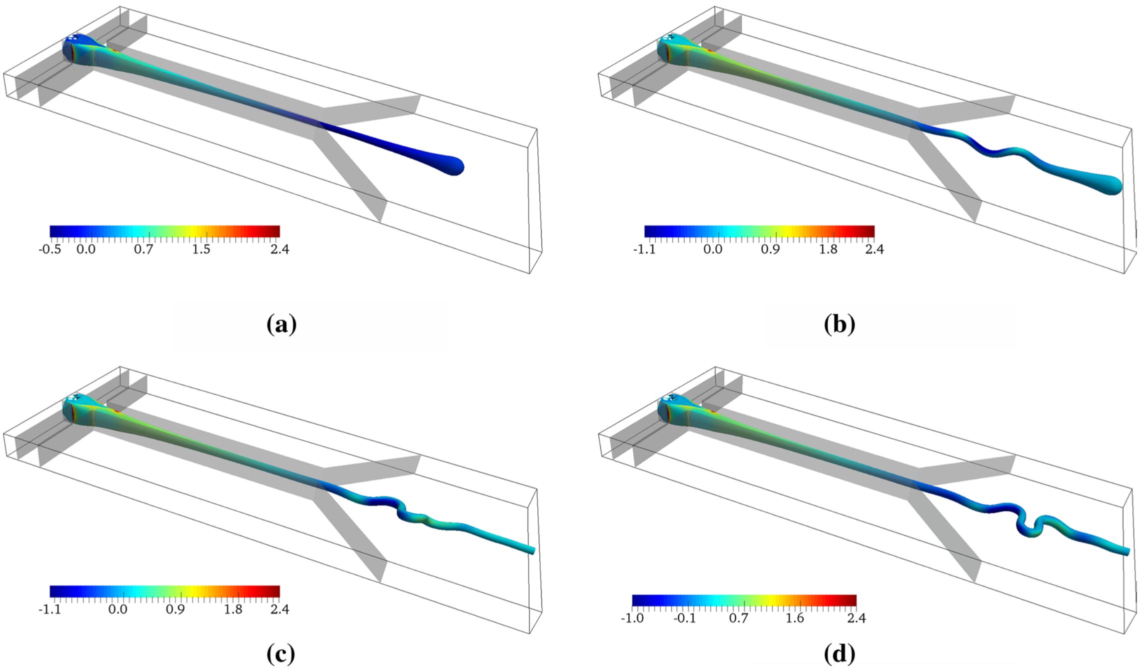

(a) **(b)** **(c)** **(d)**

Fig. 5 The flow patterns and *contours* of the dimensionless velocity derivative $(\partial u_z/\partial z)/(V_1/w)$ at different times for case 1 with $\mathrm{Re}_1 = 2.74 \times 10^{-4}, \phi = 1/12, \chi = 2174, \alpha = \pi/2$. **a** $t/(w/V_1) = 12.36$, **b** $t/(w/V_1) = 13.75$, **c** $t/(w/V_1) = 14.79$, **d** $t/(w/V_1) = 15.83$

to undergo viscous folding or buckling instability in the diverging region.

3.2 Viscous folding

The thread produced by hydrodynamic focusing continues to flow in the diverging region, and a folding instability appears due to the compressive stress. For our five simulation cases, different flow patterns have been observed. In the reference case 1 with $\mathrm{Re}_1 = 2.74 \times 10^{-4}, \phi = 1/12, \chi = 2174, \alpha = \pi/2$ as shown in Fig. 5, the thread begins to fold about an axis in the y-direction in Fig. 5b, and then the folding plane rotates in Fig. 5c. In Fig. 5d, the new folds appear mainly in the x-direction. For case 5 in which only the diverging angle is changed from $\pi/2$ to π, the flow pattern is similar to the reference case 1.

For simulation case 2 ($\mathrm{Re}_1 = 1.64 \times 10^{-3}, \phi = 1/12, \chi = 2174, \alpha = \pi/2$), as shown in Fig. 6a, the thread begins to fold in the x-direction. The folding frequency and amplitude then vary slightly after the thread exits the computation domain in Fig. 6b, and finally, the folding frequency and amplitude become stable in Fig. 6d, e. It is noted that the folding only happens in the x-direction in simulation case 2.

In case 3 with $\mathrm{Re}_1 = 2.74 \times 10^{-4}, \phi = 1/12, \chi = 1000, \alpha = \pi/2$, the onset of folding appears in the y-direction in Fig. 7b. For this case, there is not only folding instability but also strong shrinking when the thread is subject to the compressive stress. The thread is squeezed, so that the thread becomes fatter and the folding wavelength decreases as the thread flows downstream (from Fig. 7b, c). Consequently, the amplitude of newly appearing folds decreases to zero slowly and its wavelength becomes larger. Finally, the folding phenomenon disappears and the thread is completely straight in Fig. 7d.

The folding is induced by the viscous compressional stress. The velocity of the flow in the long focusing channel and near the diverging point is nearly in the z-direction, i.e., $u = (0, 0, u_z)$. Thus, the nonzero components in the viscous stress are

$$\sigma_{xz} = \frac{1}{2}\eta_i \frac{\partial u_z}{\partial x}, \tag{16}$$

$$\sigma_{yz} = \frac{1}{2}\eta_i \frac{\partial u_z}{\partial y}, \tag{17}$$

$$\sigma_{zz} = -p + \eta_i \frac{\partial u_z}{\partial z}, \tag{18}$$

where η_i is the viscosity of liquid L_1 or L_2. On the cross section of the thread, the viscous stress is longitudinal stress, $\sigma_{xz} = \sigma_{yz} = 0$ due to the plug flow. In Chung's study (Chung et al. 2010), the longitudinal stress is defined as $2\eta_i \partial u_y/\partial y$ along the centerline. In their Fig. 4d (Chung et al. 2010), the longitudinal stress is highly compressional. Here, our simulations are three dimensional, the

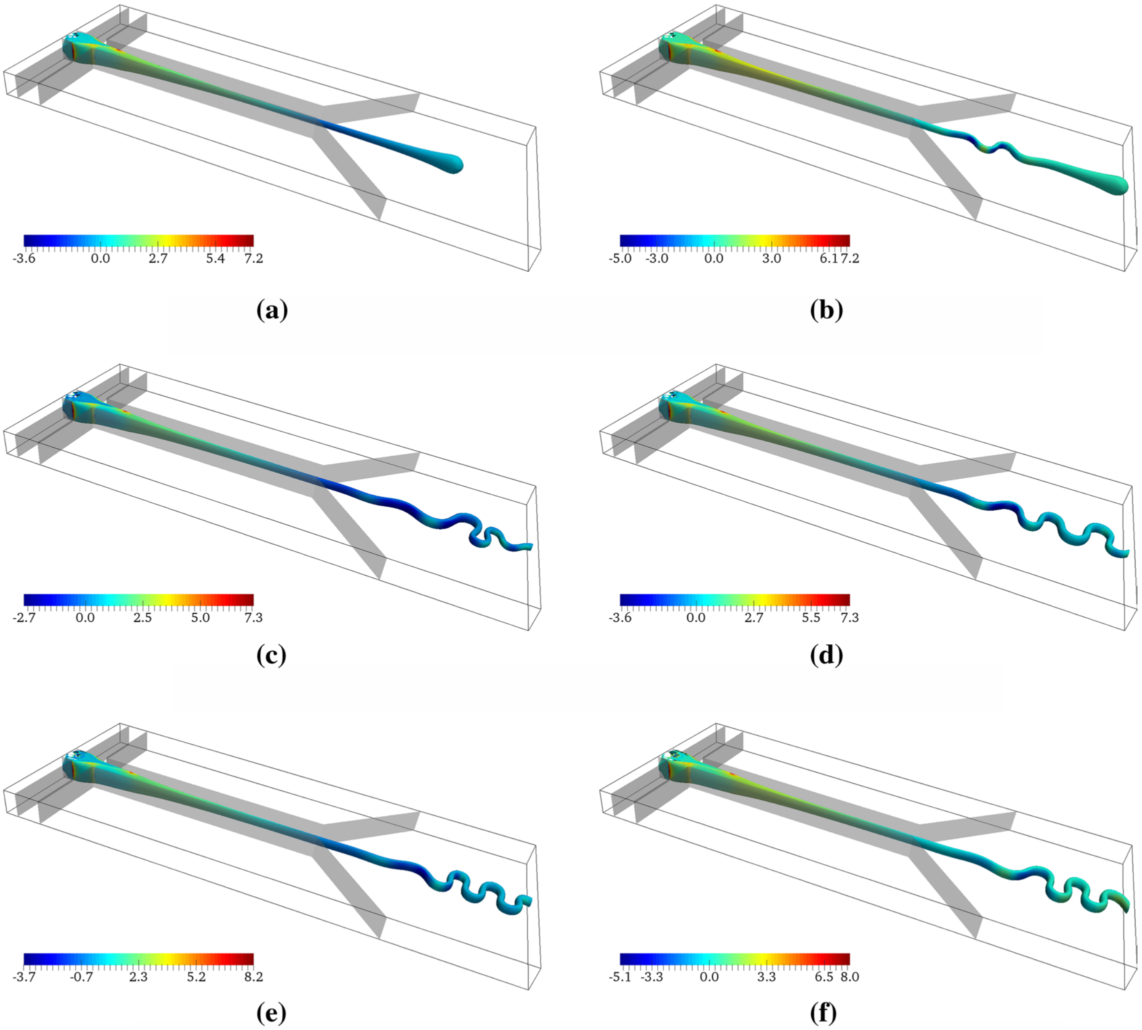

Fig. 6 The flow patterns and *contours* of the velocity derivative $(\partial u_z/\partial z)/(V_1/w)$ at different times for case 2 with $\mathrm{Re}_1 = 1.64 \times 10^{-4}, \phi = 1/12, \chi = 2174, \alpha = \pi/2$. **a** $t/(w/V_1) = 4.1$, **b** $t/(w/V_1) = 4.58$, **c** $t/(w/V_1) = 5.49$, **d** $t/(w/V_1) = 5.9$, **e** $t/(w/V_1) = 7.36$, **f** $t/(w/V_1) = 10.14$

longitudinal stress is proportional to the derivatives $\partial u_z/\partial z$. The derivatives $\partial u_z/\partial z$ of the velocity u_z with respect to z along the thread are shown in Fig. 8, and it is clear the longitudinal stress is compressional in the diverging region, especially near the diverging point.

On the thread interface, the viscous force per unit area by liquid L_2 can be obtained by $\boldsymbol{\sigma} \cdot n$, where n is the unit normal vector to the interface. Since the major axis and minor axis become stable near the diverging point, the unit normal vector is in the $x - y$ plane $n = (n_x, n_y, 0)$. Thus, the viscous force per unit area on the interface is

$$f_{\mathrm{in}} = \boldsymbol{\sigma} \cdot n = (0, 0, \sigma_{xz} n_x + \sigma_{yz} n_y) = \frac{1}{2}\eta_2 \left(0, 0, \frac{\partial u_z}{\partial n}\right). \quad (19)$$

The viscous force on the interface is proportional to the normal derivative $\partial u_z/\partial n$. Then, the bending moment on the cross section of the thread induced by the viscous force on the interface can be calculated, and it has two components

$$\omega_x = \frac{1}{2}\eta_2 \int_C \frac{\partial u_z}{\partial n}(y(s) - y_c)\mathrm{d}s, \quad (20)$$

$$\omega_y = \frac{1}{2}\eta_2 \int_C \frac{\partial u_z}{\partial n}(x(s) - x_c)\mathrm{d}s. \quad (21)$$

Where the integrals are done along the bounding line of cross section C, x_c, y_c are the coordinates of the center on the cross section. Here, the bending moment is presented by the integral part, i.e., $M_x = 2\omega_x/\eta_2$ and $M_y = 2\omega_y/\eta_2$. For case 1 with $\mathrm{Re}_1 = 2.74 \times 10^{-4}, \phi = 1/12, \chi = 2174, \alpha = \pi/2$, the bending moments of the thread M_x and M_y on the cross section at $z/w = 6.8$ are plotted from the onset of the folding instability in Fig. 8a. At first the moment M_x dominates, the cross section rotates about the x-axis resulting in

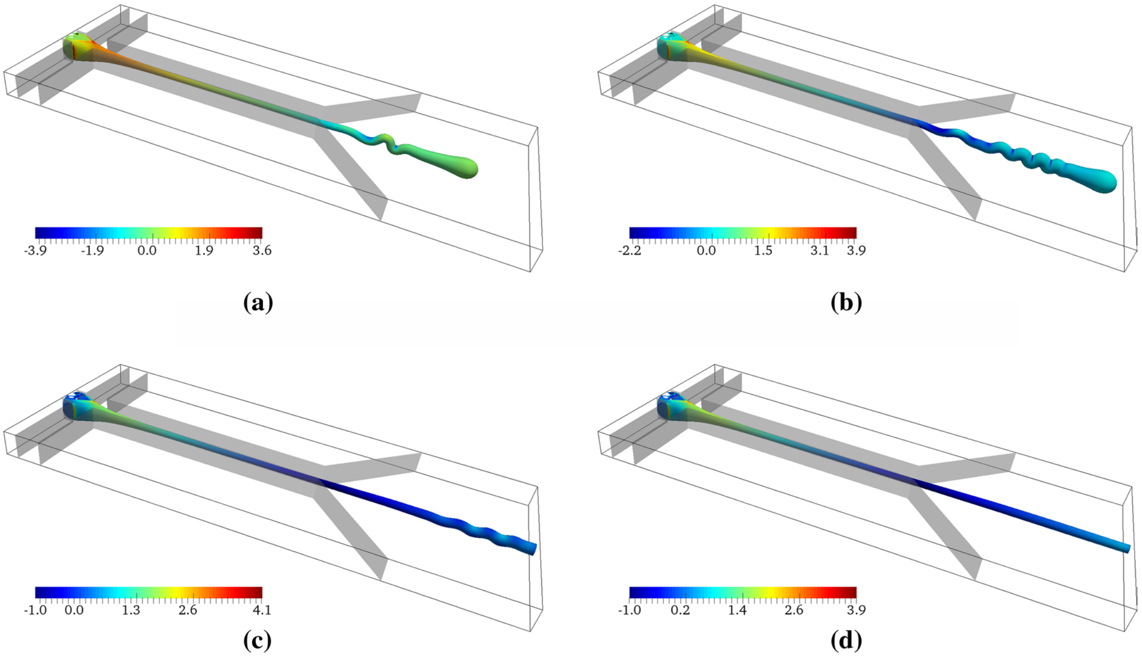

Fig. 7 The flow patterns and *contours* of the velocity derivative $(\partial u_z/\partial z)/(V_1/w)$ at different times for case 3 with $\mathrm{Re}_1 = 2.74 \times 10^{-4}, \phi = 1/12, \chi = 1000, \alpha = \pi/2$. **a** $t/(w/V_1) = 10.0$, **b** $t/(w/V_1) = 12.57$, **c** $t/(w/V_1) = 15.21$, **d** $t/(w/V_1) = 16.6$

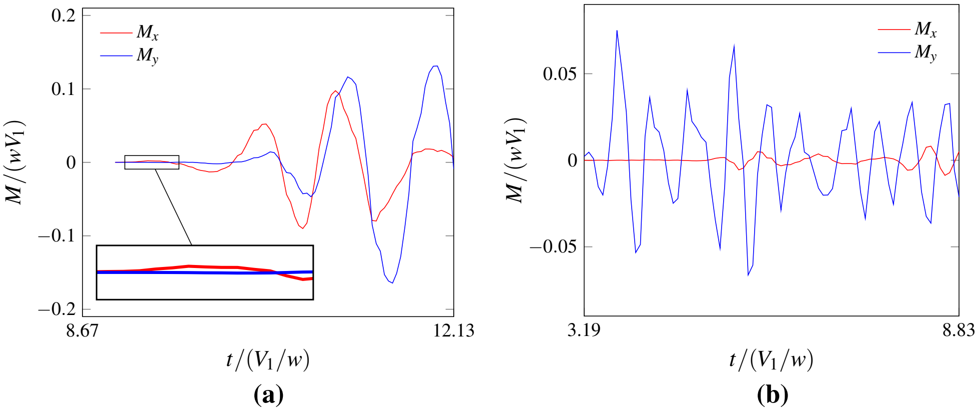

Fig. 8 The dimensionless bending moment at $z/w = 6.8$ for **a** case 1 with $\mathrm{Re}_1 = 2.74 \times 10^{-4}, \phi = 1/12, \chi = 2174, \alpha = \pi/2$ and **b** case 2 with $\mathrm{Re}_1 = 1.64 \times 10^{-3}, \phi = 1/12, \chi = 2174, \alpha = \pi/2$ when the folding instability occurs

folding in the y-direction. Then, the moment M_y increases, the folding slowly transforms via twisting to folding in the x-direction. When the ratio $\varepsilon_1/\varepsilon_2$ of the thread is much less than one the moment M_x is always very small compared to M_y, so that the folding only appears in the x-direction. This is just what we observe in simulation case 2 (similar bending moments over time are presented in Fig. 8b).

Due to the high viscosity contrast and very low Reynolds numbers involved, numerical simulations of this two-phase flow are very challenging and to our knowledge these are the first three-dimensional parallel numerical simulations of viscous threads in microchannels. However, since the computational time for these simulations is quite long, especially for such viscous threads, the simulations present only the early time onset of the buckling instability of the threads; thus, long-time comparisons with experiments for quantities such as folding amplitude and frequency are limited.

4 Conclusions

The parallel code BLUE for multiphase flows was used to simulate three-dimensional viscous folding in diverging microchannels. Liquid L_1 takes the form of a thin filament due to hydrodynamic focusing in the long channel that leads to the diverging region. The thread becomes unstable to a folding instability after its entry into the main chamber, due to the longitudinal compressive stress applied to it by the diverging flow of liquid L_2. Given the long computation time for such a low Reynolds number flow, we were limited to a parameter study comprising five simulations in which the flow rate ratio, the viscosity ratio, the Reynolds number, and the shape of the channel were varied relative to a reference model.

During the hydrodynamic focusing, the shape of the thread vary dramatically at first and then evolve slowly and finally achieve a nearly stable state, which implies that a well-developed thread is obtained in the sufficiently long focusing channel. Moreover, the cross section of the thread is elliptical rather than circular. There is a power-law relation between the dimensionless minor axis ε_1/w and the flow ratio ϕ, and our results are in good agreement with experimental and theoretical predictions of other researchers. For the major axis ε_2, the situation is more complicated. The lower viscosity ratio χ decreases the major axis, and the thread cross section appears more circular. Additionally, the interfacial tension plays important role in the thread formation after the liquid L_1 detaches from walls. Future study will be undertaken to understand the role of interfacial tension on the major axis of the thread produced by hydrodynamic focusing and the following viscous folding instability.

Unlike the previous two-dimensional simulations of Chung et al. (2010), our simulations are fully three dimensional and thus do not constrain the axis along which the folding instability could occur. The initial folding axis can be either parallel or perpendicular to the narrow dimension of the chamber. In the former case, the folding slowly transforms via twisting to perpendicular folding, or may remain parallel. The direction of folding onset is determined by the velocity profile and the ellipticity of the thread cross section in the channel that feeds the diverging part of the cell.

Due to the high viscosity contrast and very low Reynolds numbers involved, numerical simulations of this two-phase flow are very challenging and to our knowledge these are the first three-dimensional parallel numerical simulations of viscous threads in microchannels. However, since the computational time for these simulations is quite long, especially for such viscous threads, the simulations present only the early time onset of the buckling instability of the threads, thus long-time comparisons with experiments for quantities such as folding amplitude and frequency are limited. In the future, more long-time simulations with a larger range of viscosity ratio, Reynolds number, flow rate ratio and with different channel geometries will be implemented in order that exhaustive comparisons with experiments can help in improving the understanding of viscous folding in microchannels.

Acknowledgments We thank N. Ribe and T. Cubaud for helpful discussions. This work was performed using high-performance computing resources provided by the Institut du Developpement et des Ressources en Informatique Scientifique (IDRIS) of the Centre National de la Recherche Scientifique (CNRS). This research was supported by the Basic Science Research Program through the National Research Foundation of Korea (NRF) funded by the Ministry of Science, ICT and future planning (NRF-2014R1A2A1A11051346).

References

Bottausci F, Mezić I, Meinhart CD, Cardonne C (2004) Mixing in the shear superposition micromixer: three-dimensional analysis. Philos Trans R Soc Lond A Math Phys Eng Sci 362(1818):1001–1018

Bringer MR, Gerdts CJ, Song H, Tice JD, Ismagilov RF (2004) Microfluidic systems for chemical kinetics that rely on chaotic mixing in droplets. Philos Trans R Soc Lond A Math Phys Eng Sci 362(1818):1087–1104

Brun PT, Audoly B, Ribe NM, Eaves TS (2014) Liquid ropes: a geometrical model for thin viscous jets instabilities. Phys Rev Lett 114(17):174,501

Chang CC, Huang ZX, Yang RJ (2007) Three-dimensional hydrodynamic focusing in two-layer polydimethylsiloxane (pdms) microchannels. J Micromech Microeng 17(8):1479

Chen Z, Bown M, OSullivan B, MacInnes J, Allen R, Mulder M, Blom M, vant Oever R (2009) Performance analysis of a folding flow micromixer. Microfluid Nanofluidics 6(6):763–774

Chorin AJ (1968) Numerical solution of the Navier–Stokes equations. Math Comput 22(104):745–762

Chou HP, Unger MA, Quake SR (2001) A microfabricated rotary pump. Biomed Microdevices 3(4):323–330

Chung C, Choi D, Kim JM, Ahn KH, Lee SJ (2010) Numerical and experimental studies on the viscous folding in diverging microchannels. Microfluid Nanofluidics 8(6):767–776

Cruickshank J (1988) Low-reynolds-number instabilities in stagnating jet flows. J Fluid Mech 193:111–127

Cruickshank J, Munson B (1982a) An energy loss coefficient in fluid buckling. Phys Fluids (1958–1988) 25(11):1935–1937

Cruickshank J, Munson B (1982b) The viscous-gravity jet in stagnation flow. J Fluids Eng 104(3):360–362

Cruickshank J, Munson B (1983) A theoretical prediction of the fluid buckling frequency. Phys Fluids (1958–1988) 26(4):928–930

Cubaud T, Mason T (2009) High-viscosity fluid threads in weakly diffusive microfluidic systems. N J Phys 11(7):075,029

Cubaud T, Mason TG (2006a) Folding of viscous threads in diverging microchannels. Phys Rev Lett 96(11):114,501

Cubaud T, Mason TG (2006b) Folding of viscous threads in microfluidics. Phys Fluids 18(9):091,108

Cubaud T, Tatineni M, Zhong X, Ho CM (2005) Bubble dispenser in microfluidic devices. Phys Rev E 72(3):037,302

Cubaud T, Jose BM, Darvishi S (2011) Folded micro-threads: role of viscosity and interfacial tension. Phys Fluids 23(4):42,002

Griffiths R, Turner J (1988) Folding of viscous plumes impinging on a density or viscosity interface. Geophys J Int 95(2):397–419

Habibi M, Hosseini S, Khatami M, Ribe N (2014) Liquid supercoiling. Phys Fluids (1994-present) 26(2):024,101

Harlow FH, Welch JE et al (1965) Numerical calculation of time-dependent viscous incompressible flow of fluid with free surface. Phys Fluids 8(12):2182

Joseph DD, Renardy Y (1993) Fundamentals of two-fluid dynamics: part II: lubricated transport, drops and miscible liquids. Springer, Berlin

Kang TG, Hulsen MA, Anderson PD, den Toonder JM, Meijer HE (2007) Chaotic advection using passive and externally actuated particles in a serpentine channel flow. Chem Eng Sci 62(23):6677–6686

Kang TG, Hulsen MA, Anderson PD, Toonder JMd, Meijer HE (2007) Chaotic mixing induced by a magnetic chain in a rotating magnetic field. Phys Rev E Stat Nonlin Soft Matter Phys 76(6):066303

Kwak DY, Lee JS (2003) Multigrid algorithm for cell-centred finite difference method ii: discontinuous coefficient case. Department of Mathematics, KAIST, Taejon

Lee GB, Chang CC, Huang SB, Yang RJ (2006) The hydrodynamic focusing effect inside rectangular microchannels. J Micromech Microeng 16(5):1024

Mahadevan L, Ryu WS, Samuel AD (1998) Fluid'rope trick'investigated. Nature 392(6672):140

Maleki M, Habibi M, Golestanian R, Ribe N, Bonn D (2004) Liquid rope coiling on a solid surface. Phys Rev Lett 93(21):214,502

Meleson K, Graves S, Mason TG (2004) Formation of concentrated nanoemulsions by extreme shear. Soft Mater 2(2–3):109–123

Paik P, Pamula VK, Fair RB (2003) Rapid droplet mixers for digital microfluidic systems. Lab Chip 3(4):253–259

Paik P, Pamula VK, Pollack MG, Fair RB (2003) Electrowetting-based droplet mixers for microfluidic systems. Lab Chip 3(1):28–33

Peskin CS (1977) Numerical analysis of blood flow in the heart. J Comput Phys 25(3):220–252

Pollack M, Shenderov A, Fair R (2002) Electrowetting-based actuation of droplets for integrated microfluidics. Lab Chip 2(2):96–101

Ribe NM (2004) Coiling of viscous jets. In: Proceedings of the Royal Society of London A: Mathematical, Physical and Engineering Sciences, vol 460. pp 3223–3239

Ribe NM, Lister JR, Chiu-Webster S (2006) Stability of a dragged viscous thread: onset of stitching in a fluid-mechanical sewing machine. Phys Fluids 18(12):124,105

Rida A, Gijs M (2004) Manipulation of self-assembled structures of magnetic beads for microfluidic mixing and assaying. Anal Chem 76(21):6239–6246

Shin S, Juric D (2007) High order level contour reconstruction method. J Mech Sci Technol 21(2):311–326

Shin S, Juric D (2009) A hybrid interface method for three-dimensional multiphase flows based on front tracking and level set techniques. Int J Numer Methods Fluids 60(7):753–778

Shin S, Juric D (2009) Simulation of droplet impact on a solid surface using the level contour reconstruction method. J Mech Sci Technol 23(9):2434–2443

Shin S, Chergui J, Juric D (2014) A solver for massively parallel direct numerical simulation of three-dimensional multiphase flows. arXiv:1410.8568

Simonnet C, Groisman A (2005) Two-dimensional hydrodynamic focusing in a simple microfluidic device. Appl Phys Lett 87(11):114,104

Skorobogatiy M, Mahadevan L (2000) Folding of viscous sheets and filaments. EPL (Europhys Lett) 52(5):532

Stiles T, Fallon R, Vestad T, Oakey J, Marr D, Squier J, Jimenez R (2005) Hydrodynamic focusing for vacuum-pumped microfluidics. Microfluid Nanofluidics 1(3):280–283

Stroock AD, Dertinger SK, Ajdari A, Mezić I, Stone HA, Whitesides GM (2002) Chaotic mixer for microchannels. Science 295(5555):647–651

Stroock AD, Dertinger SK, Whitesides GM, Ajdari A (2002) Patterning flows using grooved surfaces. Anal Chem 74(20):5306–5312

Taylor G (1969) Instability of jets, threads, and sheets of viscous fluid. In: Applied mechanics. Springer, pp 382–388

Tchavdarov B, Yarin A, Radev S (1993) Buckling of thin liquid jets. J Fluid Mech 253:593–615

Tome MF, Mckee S (1999) Numerical simulation of viscous flow: buckling of planar jets. Int J Numer Methods Fluids 29(6):705–718

Utada A, Lorenceau E, Link D, Kaplan P, Stone H, Weitz D (2005) Monodisperse double emulsions generated from a microcapillary device. Science 308(5721):537–541

Wu Z, Nguyen NT (2005) Hydrodynamic focusing in microchannels under consideration of diffusive dispersion: theories and experiments. Sens Actuators B Chem 107(2):965–974